Modeling and Analysis of Coherent Metro + PON Converged Networks for Ultra-high Speed Applications

SAFANA AL ZOUBI[1,*] AND ROBERTO GAUDINO[1]

[1] *Politecnico di Torino, Dipartimento di Elettronica e Telecomunicazioni, Torino, Italy*
[*] *safana.alzoubi@polito.it*

Compiled March 20, 2025

To meet the ultra-high bitrates and extended-reach demands of future broadband services and 5G/6G fronthauling, today's passive optical networks (PON) requires a significant technological jump, particularly towards coherent detection. This shift makes the development of fast and accurate models for future coherent PONs essential, especially for physical-layer network planning tools and digital twin applications. In this paper, we thus present a frequency-resolved physical-based model for performance estimation of coherent transmission over PON or metro+PON converged networks, considering a broad range of electrical and optical impairments and two approaches for DSP-based equalization. Specifically, the model accounts for frequency- and polarization-dependent optical channels, optical and electrical noises, coherent receiver electrical bandwidth limitations and in-phase/quadrature imbalances. Numerical validation of the proposed frequency model against extensive time-domain simulations demonstrates high accuracy across diverse impairments, with discrepancies in the estimated signal-to-noise ratio showing a standard deviation of 0.15 dB over a very wide variation range on the relevant parameters, along with significant improvements in both time and computational efficiency. We conclude the paper by presenting two examples of application of the developed model in dimensioning ultra-high bitrates future access networks.

http://dx.doi.org/10.1364/ao.XX.XXXXXX

1. INTRODUCTION

The evolution of fronthauling (FH) requirements for advanced 5G and future 6G networks has become critical, given the high-demand applications such as high-definition video streaming, virtual reality, and the Internet of Things (IoT). These applications require new FH architectures capable of delivering high performance services over vast and usually very dense geographical landscape, which makes the wide-spread passive optical network (PON) a prospect candidate to support these requirements in which PONs are used to connect remote units for mobile applications in addition to providing fiber to the home (FTTH) residential access services [1, 2], maybe in conjunction with new architectures [3], such as an all-optical merge of the metro and access over PON segments. Current research on physical layer solutions for 100 and 200 Gbps/λ and higher bitrates future PONs debates between intensity-modulation direct-detection (IMDD) or complex modulation and coherent detection [4]. IMDD architectures, used in PON standards up to now due to their simplicity and cost-efficiency, struggle to meet the demands for ultra-high bitrates and extended reach in future access networks. These limitations has sparked a vast research interest in different flavors of coherent detection for PON, which will be a substantial leap forward, leveraging advanced modulation techniques to obtain higher bitrates together with higher receiver sensitivity, extended reach and higher number of users, albeit at the expense of increased cost and complexity compared to today's single-λ IM-DD systems, but not when compared to alternative approaches such as multi-λ IM-DD. Another future research direction involves merging the metro and access segments to simplify network architecture, enhance operational efficiency, and reduce the costs associated with transmission, detection, switching, and network management [3]. In this new and rapidly evolving context, combining the benefits of coherent PON (CPON) with converged metro-access networks necessitates fast and accurate network models and consequently effective network planning and management tools to ensure optimal performance, scalability, and cost-effectiveness, particularly for ultra-high-rate and flexible CPONs [5]. Moreover, physical layer modeling is a fundamental component in the Digital Twin, which emerged as an indispensable tool creating precise virtual replicas of physical networks, enabling comprehensive analysis and interaction with real-time networks at the higher network

level, and thus, allowing to predict, address potential issues, optimize configurations, and make data-driven decisions [6, 7].

In this paper, we thus introduce a computational- and time-efficient performance estimation tool for ultra-high speed coherent transmission over PON in the context of metro-access converged networks. Our main contribution is the presentation and numerical validation of the developed physical-based and frequency-resolved model that provides a general analytical description for relevant linear transmission impairments along optical channel and coherent receiver (CRx) together with optical and electrical noises, enabling accurate predictions of key performance metrics such as signal-to-noise ratio (SNR) and bit error rate (BER), at the output of CRx digital signal processor (DSP), also considering two variant for the receiver feed-forward adaptive equalizer. In our model, we have upgraded the work presented in [8] by comprehensively considering several CRx impairments, which are paramount for high bitrates and advanced modulation formats deploying a four-dimensional widely-linear representation (which will be discussed later [9]). Moreover, although nonlinear fiber propagation effects are an important consideration, they are typically neglected in short-range networks such as PON. If targeting wavelength division multiplexing (WDM) with relatively long-reach networks, these effects can be modeled as additional Gaussian Noise (GN-models) and incorporated into the generalized optical to signal ratio (G-OSNR). As such, they are not included within the scope of this manuscript; however, the developed frequency model can be extended to account for these effects.

The paper is organized as follows: Sect. 2 details the development of a performance estimation tool based on a frequency-resolved model that considers the physical layer characteristics of coherent transmission under several possible impairments. In Sect. 3, we discuss the validation of the model's accuracy across various parameters and scenarios, supported by a statistical analysis, while Sect. 4 demonstrates a practical application of the developed model for dimensioning ultra-high flexible future converged metro+PON scenarios.

2. ANALYTICAL MODELING OF COHERENT TRANSMISSION

We consider a standard full dual-polarization (DP) CRx as depicted in Fig. 1, where the received optical signal first passes through a polarization beam splitter (PBS), separating it into two polarizations. Each polarization is then combined with the local oscillator (LO) signal using a 90° optical hybrid. The resulting eight signals are subsequently detected by four balanced photo diodes (PDs) pairs, forming four electrical signals. These signals are then amplified by transimpedance amplifiers (TIAs) and converted to digital signals by analog-to-digital converters (ADCs) before undergoing DSP operations. In the following, we will introduce equations that describe the input-output relationships for each of these components individually, where relevant, and subsequently address the associated noise contributions. The ultimate goal of this section is to establish a set of equations in the frequency domain that enables the evaluation of both signal and noise power spectral densities (PSDs) in the presence of various physical layer linear non-idealities commonly encountered in the CRx, such as asymmetry, time-skew, and bandwidth limitations. The availability of signal and noise PSDs in closed form will then allow in Sect. 3 to analytically evaluate the resulting spectrally resolved SNR and then the BER.

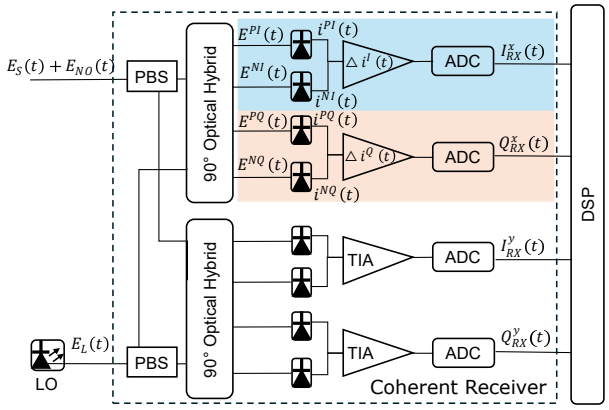

Fig. 1. Block diagram of the dual-polarization coherent receiver. LO: local oscillator, PBS: polarization-beam splitter, TIA: transimpedance amplifier, ADC: analog-to-digital converter, and DSP: digital signal-processing circuit.

A. Physical-based Characterization of the Coherent Receiver

We start by assuming an ideal PBS followed by a 90° optical hybrid, which may be unbalanced but is assumed to have an infinite bandwidth as it is usually the case within the optical range (filtering will be addressed later). For each polarization (i.e. x or y), at the output of the PBS, the terms $E_S(t)+E_{NO}(t)$ and $E_L(t)$ denote the received optical signal accompanied by optical noise and the LO signal, respectively. The hybrid's four output optical signals are related to the two input signals through its complex transmission coefficients [10], as follows:

$$\begin{bmatrix} E^{PI}(t) \\ E^{NI}(t) \\ E^{PQ}(t) \\ E^{NQ}(t) \end{bmatrix}_{x,y} = \begin{bmatrix} s_1^{PI} & s_2^{PI} \\ s_1^{NI} & -s_2^{NI} \\ s_1^{PQ} & js_2^{PQ} \\ s_1^{NQ} & -js_2^{NQ} \end{bmatrix}_{x,y} \cdot \begin{bmatrix} E_S(t)+E_{NO}(t) \\ E_L(t) \end{bmatrix}_{x,y}, \quad (1)$$

where the parameters s represent the optical hybrid coefficients, with the superscripts corresponding to P, N to indicate the signal path towards the two PDs in each balanced PD, while I, Q indicate the inphase and quadrature components, respectively. The hybrid output signals $E_{PI}(t)$, $E_{NI}(t)$, $E_{PQ}(t)$, and $E_{NQ}(t)$ are the input signals of the P and N PDs for the I and Q components, respectively. In an ideal optical hybrid, all the s parameters in Eq.1 matrix equals 0.5 (which would lead to the target 0.25 splitting in signal power); however, in our model, s is allowed to be a complex number, introducing both phase and amplitude imbalances between the signal paths inside the optical hybrid. In the following equations, we derive the I and Q components on each of the polarization's branches (temporarily omitting the time notation from the mathematical representation of E for the sake of space). The detected photocurrent at the output, for instance, of the P-PD of the I component is the squared modulus of the input optical signals, assuming a band-limited PD, and is given by:

$$i^{PI}(t) = h^{PI}\left(t-\tau^{PI}\right) \otimes R^{PI}\left|s_1^{PI}\left(E_S+E_{NO}\right)+s_2^{PI}E_L\right|^2, \quad (2)$$

where $h^{PI}(t)$ is the impulse response of the P-PD up to the current subtraction in the TIA [11], τ^{PI} the time delay associated with the respective path, R^{PI} the PD responsivity to the applied

signal. The superscript denotes the corresponding signal path (PI in this case), and $\otimes$ denotes convolution. Equation 2 can thus be rewritten as:

$$\begin{aligned} i^{PI}(t) = h^{PI}\left(t-\tau^{PI}\right) \otimes R^{PI}\Big(& s_1^{PI}s_2^{PI*}E_S E_L^* + s_1^{PI*}s_2^{PI}E_S^*E_L \\ &+ s_1^{PI}s_2^{PI*}E_{NO}E_L^* + s_1^{PI*}s_2^{PI}E_{NO}^*E_L + \left|s_1^{PI}\right|^2 E_S E_{NO}^* \\ &+ \left|s_1^{PI}\right|^2 E_S^* E_{NO} + \left|s_1^{PI}E_S\right|^2 + \left|s_2^{PI}E_L\right|^2 + \left|s_1^{PI}E_{NO}\right|^2\Big), \end{aligned} \tag{3}$$

where $*$ represents complex conjugate operation. Subsequently, neglecting the terms that are not associated with LO since the LO power is expected to be dominant in these unamplified systems, and introducing the following notation $s_1^{PI}s_2^{PI*} = s^{PI} = \Re\{s^{PI}\} + j\Im\{s^{PI}\}$, where $\Re$ and $\Im$ are the real and imaginary notations, we can write:

$$\begin{aligned} i^{PI}(t) = h^{PI}\left(t-\tau^{PI}\right) \otimes R^{PI}\Big(& 2\Re\left\{s^{PI}\right\}\Re\{E_S E_L^*\} \\ &- 2\Im\left\{s^{PI}\right\}\Im\{E_S E_L^*\} + 2\Re\left\{s^{PI}\right\}\Re\{E_{NO}E_L^*\} \\ &- 2\Im\left\{s^{PI}\right\}\Im\{E_{NO}E_L^*\} + \left|s_2^{PI}E_L\right|^2\Big), \end{aligned} \tag{4}$$

The current at the output of the N-PD will then have the following similar expression:

$$\begin{aligned} i^{NI}(t) = h^{NI}\left(t-\tau^{NI}\right) \otimes R^{NI}\Big(& \\ &- \left(2\Re\left\{s^{NI}\right\}\Re\{E_S E_L^*\} - 2\Im\left\{s^{NI}\right\}\Im\{E_S E_L^*\}\right) \\ &- \left(2\Re\left\{s^{NI}\right\}\Re\{E_{NO}E_L^*\} - 2\Im\left\{s^{NI}\right\}\Im\{E_{NO}E_L^*\}\right) \\ &+ \left|s_2^{NI}E_L\right|^2\Big), \end{aligned} \tag{5}$$

This yields the differential photocurrent for the I component as:

$$\begin{aligned} \Delta i^I(t) =& h_{BPD}^{II}(t) \otimes \Re\{E_S E_L^*\} + h_{BPD}^{IQ}(t) \otimes \Im\{E_S E_L^*\} + \\ & h_{BPD}^{II}(t) \otimes \Re\{E_{NO}E_L^*\} + h_{BPD}^{IQ}(t) \otimes \Im\{E_{NO}E_L^*\} \\ & + h_{LO}^{I}(t) \otimes |E_L|^2, \end{aligned} \tag{6}$$

where h_{BPD}^{II} and h_{BPD}^{IQ}, further detailed in the Appendix, are the balanced photodetection impulse responses composing the I photocurrent with respect to the real and imaginary components of the received optical signal. It should be noted that for an ideal optical hybrid, the s parameters are real, resulting in $h_{BPD}^{IQ} = 0$ eliminating the contribution of the received signal's imaginary part to the detected I photocurrent. On the other hand, h_{LO}^{I} is the local oscillator impulse response, which is effectively canceled out in an ideal balanced detection setup where the P and N paths are identical. Similarly, the differential photocurrent for the Q component is defined as:

$$\begin{aligned} \Delta i^Q(t) =& h_{BPD}^{QI}(t) \otimes \Re\{E_S E_L^*\} + h_{BPD}^{QQ}(t) \otimes \Im\{E_S E_L^*\} + \\ & h_{BPD}^{QI}(t) \otimes \Re\{E_{NO}E_L^*\} + h_{BPD}^{QQ}(t) \otimes \Im\{E_{NO}E_L^*\} \\ & + h_{LO}^{Q}(t) \otimes |E_L|^2, \end{aligned} \tag{7}$$

After balanced photodetection, shot noise from both photodiodes is introduced to the resulting differential photocurrent, which then passes through the TIA modeled as a band-limited low-pass filter and additive thermal noise. Lastly, the current passes through the ADC, which is similarly modeled as a band-limited low-pass filter, followed by a quantizer. This yields the signal for the I component at the input of the DSP, where we reintroduce the polarization notation as follows:

$$\begin{aligned} I^x(t) =& h_{ADC}^{I,x}(t) \otimes \\ & \left(h_{TIA}^{I,x}(t) \otimes \left(\Delta i^{I,x}(t) + n_{sh}^{I,x}(t)\right) + n_{th}^{I,x}(t)\right) + n_{ADC}^{I,x}(t), \end{aligned} \tag{8}$$

where h_{TIA} and h_{ADC} represent the impulse responses of the TIA and ADC for their respective signal paths, in this case, I, x the I component of the x polarization. Similarly, n_{sh}, n_{th}, and n_{ADC} are shot, thermal and quantization noises, respectively, for their corresponding signal paths (defined in more detail later in Sect. 3.A.1). Assuming that the frequency difference between the transmitter and the local oscillator will be corrected in the DSP, the terms $\Re\{E_S E_L^*\}$ and $\Im\{E_S E_L^*\}$ can be written as $\sqrt{P_L}I$ and $\sqrt{P_L}Q$, respectively, where P_L is the LO power. Finally, the four CRx outputs after the ADCs can be expressed in a 4-D time-domain vector as follows:

$$\begin{aligned} \begin{bmatrix} I^x(t) \\ Q^x(t) \\ I^y(t) \\ Q^y(t) \end{bmatrix}_{RX} &= \mathbf{h}_{ADC}(t) \otimes \mathbf{h}_{TIA}(t) \otimes \mathbf{h}_{BPD}(t) \\ \otimes \sqrt{P_L}&\left(\begin{bmatrix} I^x(t) \\ Q^x(t) \\ I^y(t) \\ Q^y(t) \end{bmatrix}_S + \begin{bmatrix} I^x(t) \\ Q^x(t) \\ I^y(t) \\ Q^y(t) \end{bmatrix}_{NO}\right) + \begin{bmatrix} n_{RX}^{I,x}(t) \\ n_{RX}^{Q,x}(t) \\ n_{RX}^{I,y}(t) \\ n_{RX}^{Q,y}(t) \end{bmatrix}, \end{aligned} \tag{9}$$

The time-domain matrices $\mathbf{h}_{ADC}$, $\mathbf{h}_{TIA}$, and $\mathbf{h}_{BPD}$, defined in Appendix A, are 4-D matrices representing the impulse responses for the four signal paths in the CRx. The second term denotes the CRx noise, also defined in Appendix A, which includes local oscillator relative intensity noise, shot noise, thermal noise, and quantization noise. Finally, by adopting the widely-linear transformation, which establishes equivalent relations between linear transformations in real vector spaces and those in complex vector spaces as explained in [9], Eq. 9 can be modified to express the received signal at the input of the DSP as $\mathbf{E}_{RX} = \begin{bmatrix} E^x & E^{x*} & E^y & E^{y*} \end{bmatrix}_{RX}^T$:

$$\begin{bmatrix} E^x \\ E^{x*} \\ E^y \\ E^{y*} \end{bmatrix}_{RX} = \mathbf{h}_{RX}(t) \otimes \left(\begin{bmatrix} E^x \\ E^{x*} \\ E^y \\ E^{y*} \end{bmatrix}_S + \begin{bmatrix} E^x \\ E^{x*} \\ E^y \\ E^{y*} \end{bmatrix}_{NO}\right) + \mathbf{n}_{RX}(t), \tag{10}$$

where $\mathbf{h}_{RX}(t)$ and $\mathbf{n}_{RX}(t)$, defined in Appendix A, represent the physical-based 4-D widely-linear characterization of the CRx response and electrical noises, respectively, and $E^{x/y} = I^{x/y} + jQ^{x/y}$

B. Introducing the typical filtering and noises in Metro+PON Networks

As this study examines coherent transmission in a converged metro-access network, Fig. 2 depicts a possible downstream network configuration, in which the metro segment is all-optically

connected to PON through reconfigurable optical add-drop multiplexers (ROADMs), as it was for instance experimentally studied in [3]. Here, we focus on the downstream (DS) transmission; however, symmetrical considerations can be applied to the upstream (US). It is important to note, though, that the model cannot natively account for impairments generated by burst-mode US transmission. In this subsection, we will add to the previously introduced model the resulting optical filtering effects and the noises that are typically present on the link.

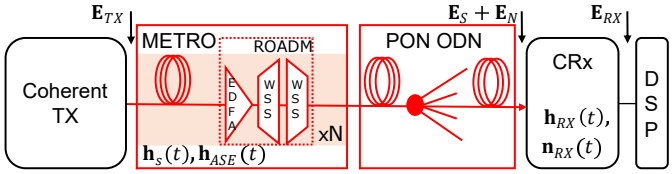

Fig. 2. Coherent transmission over converged metro-access optical network configuration. EDFA: Erbium-Doped fiber amplifier. WSS: wavelength-selective switch. PON: passive optical network. ODN: optical distribution network. CRx: coherent receiver. DSP: digital signal processor.

This study builds upon and largely extend the research detailed in [8], in which the authors modeled the optical propagation link as a generic 2 by 2 frequency- and polarization-dependent transfer function acting on the transmitted signal in addition to additive Gaussian optical noise, followed by coherent detection and a minimum mean-square error (MMSE)-based feed forward equalizer (FFE). In their study, they calculate the spectral signal to noise ratio (SNR) at the input of the equalizer in the DSP and consequently the SNR after the equalizer following the analytics described in [12]. In our upgraded analysis, we consider a similar optical link model but representing it in the widely-linear 4 by 4, since this approach, as we started to show in Sect. 2.A and as we will further elaborate here, is the form that allows to account for IQ imbalances in the CRx.

The metro segment here is assumed to consist of multiple spans ($\times N$ in Fig. 2), where the overall frequency- and polarization- dependent optical channel impulse response is denoted as the 2x2 impulse response $\mathbf{h}_s(t)$ (which in the final equations will be converted to the more commonly used optical 2x2 Jones frequency transfer function). This response can be completely general, accounting for any polarization-dependent loss (PDL), any generic 2 by 2 random unitary Jones matrix (accounting for random fiber birefringence) and any optical filtering within the ROADMs wavelength-selective switch (WSS). The transmitted optical signal $\mathbf{E}_{TX}$ propagates through the optical channel, then it is received at the input of CRx as $\mathbf{E}_s = \mathbf{h}_s(t) \otimes \mathbf{E}_{TX}$. In this scenario, amplified spontaneous emission (ASE) noise is introduced by optical amplifiers namely (Erbium-Doped fiber amplifiers (EDFAs)) placed inside the ROADMs and characterized by a gain equal to the span loss and a corresponding noise PSD, and both are assumed as frequency-flat over the bandwidth of the modulated optical signal. These noise sources are then affected by PDL and shaped by filtering effects in ROADMs. Thus, the total impulse response associated with this process is represented as another frequency- and polarization-dependent relation expressed by the 2x2 impulse response $\mathbf{h}_{ASE}(t)$, enabling to consider also colored ASE noise at the input of CRx expressed as $\mathbf{E}_{NO} = \mathbf{h}_{ASE}(t) \otimes N(t)$, where $N(t)$ is the optical noise added in the metro segment. The final step for this subsection is to convert Equation 10 in the frequency domain and add the aforementioned impairments in their widely-linear 4 by 4 form, leading to:

$$\begin{bmatrix} E^x(f) \\ E^{x*}(-f) \\ E^y(f) \\ E^{y*}(-f) \end{bmatrix}_{RX} = \mathbf{H}_{RX}(f)\,\mathbf{H}_s(f) \begin{bmatrix} E^x(f) \\ E^{x*}(-f) \\ E^y(f) \\ E^{y*}(-f) \end{bmatrix}_{TX} + \mathbf{H}_{RX}(f)\,\mathbf{H}_{ASE}(f) \begin{bmatrix} n^x(f) \\ n^{x*}(-f) \\ n^y(f) \\ n^{y*}(-f) \end{bmatrix}_{ASE} + \mathbf{N}_{RX}(f), \tag{11}$$

C. Equalization and Performance Evaluation

Following the methodology outlined in [8] (and assuming the resulting matrix $\mathbf{H}_{RX}(f)\,\mathbf{H}_s(f)$ is an invertible matrix at any frequency inside the useful signal bandwidth, which is always verified in actual systems), we assume a DSP-based adaptive equalizer that can compensate for the channel response by applying its 4 by 4 inverse, which is achieved in practical CRx implementations through a 4 by 4 real-valued multiple-input multiple-output (MIMO) adaptive FFE, yielding:

$$\begin{bmatrix} E^x(f) \\ E^{x*}(-f) \\ E^y(f) \\ E^{y*}(-f) \end{bmatrix}_{EQ} = \begin{bmatrix} E^x(f) \\ E^{x*}(-f) \\ E^y(f) \\ E^{y*}(-f) \end{bmatrix}_{TX} + \mathbf{H}_s^{-1}(f)\,\mathbf{H}_{ASE}(f) \begin{bmatrix} n^x(f) \\ n^{x*}(-f) \\ n^y(f) \\ n^{y*}(-f) \end{bmatrix}_{ASE} + \mathbf{H}_s^{-1}(f)\,\mathbf{H}_{RX}^{-1}(f)\,\mathbf{N}_{RX}(f), \tag{12}$$

In Eq.12, the equalized signal clearly depends on the frequency responses of the optical channel and CRx considering optical and electrical noises. This yields the spectrally-resolved SNRs from translating Eq.12 into the related PSDs for the signals and noises on the two polarizations (assuming that the transmitted signal is strongly circular [13] and the signals/noises on both polarization are statistically independent [8]). Conversely, when considering a 2 by 2 complex-valued MIMO adaptive FFE in practical CRx, in the presence of a 4-D overall response, we

introduce the 4-D matrix $\mathbf{H}^{-1}$ to Eq. 11 as follows:

$$\begin{bmatrix} E^x(f) \\ E^{x*}(-f) \\ E^y(f) \\ E^{y*}(-f) \end{bmatrix}_{EQ} = \mathbf{H}^{-1}(f)\mathbf{H}_{RX}(f)\,\mathbf{H}_s(f) \begin{bmatrix} E^x(f) \\ E^{x*}(-f) \\ E^y(f) \\ E^{y*}(-f) \end{bmatrix}_{TX} + \mathbf{H}^{-1}(f)\mathbf{H}_{RX}(f)\,\mathbf{H}_{ASE}(f) \begin{bmatrix} n^x(f) \\ n^{x*}(-f) \\ n^y(f) \\ n^{y*}(-f) \end{bmatrix}_{ASE} + \mathbf{H}^{-1}(f)\mathbf{N}_{RX}(f), \quad \textbf{(13)}$$

where $\mathbf{H}^{-1}$, defined in Appendix A, is the inverse of the partial 2 by 2 response taken from the overall response $\mathbf{H}_{RX}(f)\,\mathbf{H}_s(f)$, deployed in a 4-D form. Here, the equalized signal in one polarization includes components of the transmitted signal along with interference terms from its conjugate and the other polarization. Therefore, only the term directly related to the signal is considered the desired component, while the other elements—those related to the signal's conjugate, the second polarization, and its conjugate—are treated as interference (added to noises), thereby calculating the resulting spectral SNR in the presence of inphase quadrature (IQ) mixing accordingly [13]. This spectral SNR is then applied in the analytical tool presented in [12] to determine the SNR after equalization.

In summary, Eq. 12 and 13, along with the formulas (1,2,3) in [8], enable us to estimate the SNR after equalization and, consequently, the BER performance over a wide range of linear impairments in both the optical link and the receiver. This includes various types of optical and electrical filtering, possible imbalances within the CRx, as well as different types of (spectrally-dependent) noises.

3. ANALYTICAL MODEL VALIDATION AND ACCURACY

This section is fully focused on validating the accuracy of our proposed model in several practical situations. We begin by validating it across diverse parameters of coherent transmission over metro+PON network, followed by a more general statistical analysis. Various imperfections are analyzed for both the CRx and the optical channel: specifically, for the CRx, these include electrical noises, receiver electrical bandwidth limitations, IQ imbalances, and time skew. Additionally, for the optical channel, optical filtering, polarization rotation, PDL, and ASE noise are addressed. The validation is carried out by comparing our developed frequency-resolved model (indicated as the "frequency simulator" in the following) to extensive time-domain simulations (time simulator in the following, see [14]) in terms of estimated performance (SNR, BER) and required CPU-time.

The frequency simulator computes $SNR(f)$ by first evaluating the PSDs of the signal and noise terms in Eq. 12 or 13, and then determining the resulting SNR at the receiver equalizer output based on [12]. The time simulations are conducted under the same transmission conditions, utilizing a T/2-spaced 4 by 4 or 2 by 2 MIMO FFE for equalization and polarization demultiplexing, that employs the least mean square (LMS) algorithm, operating at 2 samples per symbol. The time simulations run on a pattern length of 2^{17} transmitted symbols for 10 repetitions. The SNR is computed at the output of the CRx FFE as the ratio of the average signal energy to the mean square error of the received symbols. Subsequently, for both simulators, the BER is calculated according to the modulation format, as detailed in [15]. For example, for M-quadrature amplitude modulation (M-QAM), the BER is determined as follows:

$$BER = \frac{4}{\log_2(M)}\left(1-\frac{1}{\sqrt{M}}\right)\frac{1}{2}\mathrm{erfc}\left(\sqrt{\frac{3SNR}{2(M-1)}}\right), \quad \textbf{(14)}$$

where M is the modulation order. The developed model is validated in two configurations: the first is a back-to-back (BtB) setup that includes optical noise loading and several CRx non-idealities, and the second involves a converged metro-access setup, incorporating optical filtering and polarization effects into the performance estimation along with BtB impairments. Finally, we statistically validate the proposed frequency model by randomly varying the optical network and CRx parameters and evaluating its performance estimation accuracy.

A. Model Validation in a Back to Back Setup

In this section, we investigate the proposed model validity in a BtB coherent transmission setup with optical noise loading. The analysis begins by defining and validating the model's performance concerning CRx electrical noises, followed by an evaluation of bandwidth limitations and IQ imbalances.

A.1. Coherent Receiver Electrical Noises

As already pointed out in Sect. 2, various sources of electrical noise are present at the CRx and are especially critical in unamplified coherent transmission systems. We start by defining these noise sources, beginning with shot noise, typically described as a stationary random process approximated by Gaussian statistics with a variance in each PD of $\sigma^2_{shot} = 2q(RP)\Delta f$, where q is the electron charge, R is the PD responsivity, P is the power incident on the PD (i.e. the received optical power (ROP) and LO power), and Δf is the effective bandwidth. Secondly, thermal noise variance defined in each amplifier as $\sigma^2_{TIA} = i^2_{TIA}\Delta f$, where i_{TIA} is the equivalent TIA input-referred noise current density [11, 16]. The third considered noise source is the relative intensity noise (RIN) of the local oscillator, where amplitude instability defined by the RIN in the LO introduces interference to the resulting current; while it is ideally rejected in balanced detection, in our considered non-ideal balanced receivers' common mode rejection ratio (CMRR) determines the amount of introduced RIN. CMRR depends on the P- and N-path differences, and particularly on two factors: the power imbalance (e.g., differences in photodiode responsivity, as considered in this manuscript), which is frequency-independent, and the time skew (τ^{PI} not equal to τ^{NI} in Eq. 6), which is frequency-dependent [16]. Lastly, quantization noise, introduced by the ADC digitization, is modeled as white and additive (valid only for sufficiently high resolutions, i.e. when effective number of bits (ENOB) is at least 4 bits or higher [17]). ADC variance is defined as $\sigma^2_{ADC} \simeq \Delta^2/12$, where Δ is the quantization step-size expressed as $\sqrt{\sigma_x^2.10^{PAPR/10}}\Big/2^{ENOB-1}$, where σ_x and $PAPR$ are the ADC input signal variance and peak of average power ratio (PAPR). It should be noted that PAPR depends on the modulation format, signal pulse shaping parameters such as roll-off factor [18], in addition to other factors related to filtering and chromatic dispersion [19], therefore, the typical PAPR values for each modulation and roll-off were estimated using time simulations and applied in the previous formula to address

quantization noise in the frequency simulator.

Simulation Setup: Throughout the paper analysis, unless stated otherwise, the transmitted signal is a DP M-QAM signal shaped by a square-root raised cosine filter with a roll-off factor of 0.2 and an average transmitted power of 11 dBm. Optical noise is introduced to the signal prior to coherent detection, followed by various CRx imperfections. The physical parameters of the CRx are based on [20], which introduce the following electrical noises: shot noise with a PD responsivity value of 0.62, thermal noise with a 19 pA/$\sqrt{Hz}$ as the value of TIA current, RIN with a value of −145 dB/Hz, −21.6 as CMRR in dB, LO power of 14 dBm, and quantization noise with 5 bits as the ENOB. CRx bandwidth limitations and IQ imbalances are incorporated into the analysis where specifically mentioned. Likewise, optical and polarization effects are stated based on the specific objectives of each section. All simulations are run on a laptop with a 1.70 GHz 13th Gen Intel Core i7-1355U CPU and 16 Gbytes RAM. Both simulations have the same resolution, meaning they evaluate the same studied points under exact conditions and parameter sets. For presentation purposes—applied consistently across all relevant figures—the frequency simulator results are represented with lines, while the time simulator results are depicted with markers.

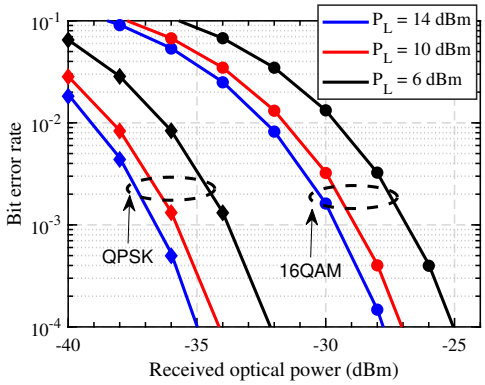

Fig. 3. Bit error rate versus received optical power in a back to back setup for various local oscillator powers and modulation formats. Lines are frequency simulator and markers are time simulator results.

Figure 3 illustrates the *BER* versus received optical power for coherent transmission in a BtB configuration corresponding to various LO powers and two modulation formats, i.e. quadrature phase shift keying (QPSK) and 16-QAM, where the frequency simulator results are plotted in comparison to time simulator. The previously described transmitted signal is a 28 Gbaud signal with no added optical noise. The CRx imperfections include all electrical noises, no bandwidth limitations or IQ imbalances. The results demonstrate high accuracy between the two simulators, irrespective of LO power and modulation format. The required CPU-time for the two evaluations is anyway enormously different, as we will better detail later with some examples. This is the key rationale behind our proposed frequency-domain model, targeted for obtaining system performance estimation in fractions of a second of CPU time and thus potentially suitable for network planning tools, optimizers and orchestrators.

Next, with the received 28 Gbaud DP-QPSK signal power set at −33 dBm, in Fig. 4, we analyze the impact of varying the receiver thermal noise, i.e. the TIA current, while keeping other

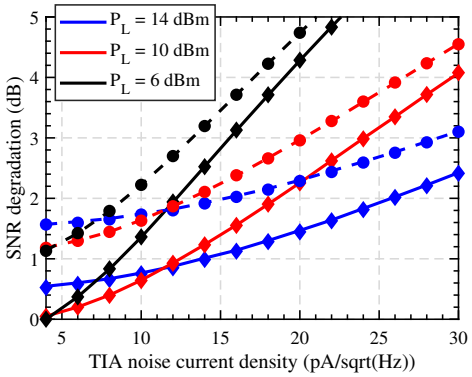

Fig. 4. SNR degradation versus TIA input-referred noise current density for various Local oscillator power with and without optical noise. Lines: frequency simulator, markers: time simulator, Solid: Infinity OSNR, dashed: 20 dB of OSNR defined on a bandwidth equal to the signal symbol-rate.

noise sources constant. Here, we define SNR degradation as the difference between the estimated SNR and the maximum SNR value observed after equalization in the particular figure. Figure 4 illustrates the SNR degradation after equalization for different LO powers and two Optical SNR (OSNR) values, as evaluated by both frequency and time simulators. As illustrated, the results from both simulators show again very good agreement across various LO powers and OSNR values (i.e. the time-domain dotter markers are completely superimposed to the frequency-domain results represented as lines). Several system considerations can be obtained from graphs such as those presented in Fig. 4: for instance, for an OSNR of 20 dB, defined on a bandwidth equal to the symbol-rate, a penalty of about 1 dB is observed at low TIA current values, while this penalty decreases to about 0.5 dB for higher TIA current values, such as 30 pA/sqrt(Hz). For lower TIA current values, specifically 4 pA/sqrt(Hz), increasing the LO power results in a higher penalty in the estimated SNR, which can be explained by the increased LO amplitude noise with respect to a fixed signal power. In contrast, for TIA current values exceeding 12 pA/sqrt(Hz), a higher LO power reduced the SNR penalty versus TIA current as it enhances the signal power, thereby mitigating the impact of thermal noise.

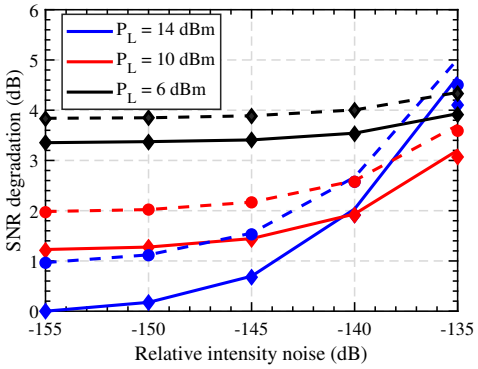

Fig. 5. SNR degradation versus RIN values for various Local oscillator power values with and without optical noise. Lines: frequency simulator, markers: time simulator, Solid: Infinity OSNR, dashed: 20 dB of OSNR.

Similarly, Fig. 5 demonstrates the effect of RIN on the estimated SNR penalty, as assessed by both the frequency and time simulators for various LO powers and OSNR values. The results show great agreement between the two simulators, with a minor discrepancy of approximately 0.4 dB observed only at high RIN values combined with high LO power. At an OSNR of 20 dB, the SNR penalty ranges from about 0.2 to 1 dB, increasing with higher LO power and lower RIN values. As illustrated, for low RIN values, increasing the LO power results in a reduced SNR penalty. In contrast, for high RIN values, a higher LO power exacerbates the SNR penalty.

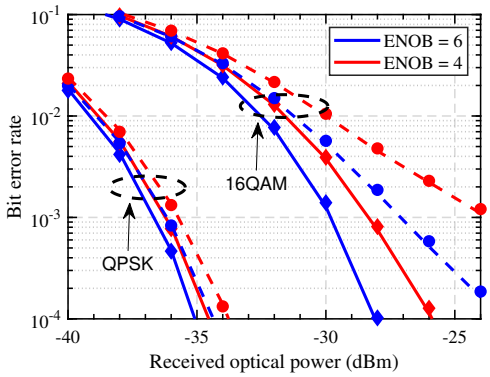

Fig. 6. Bit error rate versus received optical power corresponding to ADC effective number of bits, OSNR and modulation formats. Lines: frequency simulator, markers: time simulator, Solid: Infinity OSNR, dashed: 20 dB of OSNR defined on a bandwidth equal to the signal symbol-rate.

Figure 6 illustrates the impact of quantization noise on the system performance, as indicated by the *BER* as a function of the received optical power, considering ADC ENOB, OSNR values, and modulation format. The estimated *BER* values from both simulators exhibit again a good agreement across all values. As seen, to achieve a *BER* value of 10^{-2}, reducing the ENOB from 6 to 4 requires an increase of the ROP by 1 dB for the 16-QAM modulation format at both OSNR values. In contrast, for QPSK, changing the ENOB has a minimal effect on the required ROP for the same BER.

The CPU time required to generate all data points in Fig. 6 was about 12 seconds with the frequency domain simulator, compared to about 44 minutes for the time-domain simulations. This "CPU-time gain" of a factor higher than 200x, demonstrates the significant efficiency in time and computational resources afforded by our developed model for accurately estimating network performance.

A.2. Coherent Receiver Bandwidth Limitations

In the developed frequency model, all components, including CRx PDs, TIAs, and ADCs, are defined by their frequency responses. When included in the simulation, we assume that these responses are modeled as first-order low-pass super-Gaussian filters with predefined 3-dB bandwidths. The order and bandwidth of these frequency responses can be varied to assess their impact on the overall performance estimation.

Figure 7 shows the CRx frequency-dependent performance, quantified by the SNR degradation, as a function of bandwidth limitations in the CRx electrical components. This analysis considers both the individual effects of the CRx components and their combined impact on a 50 Gbaud DP-QPSK transmission, as

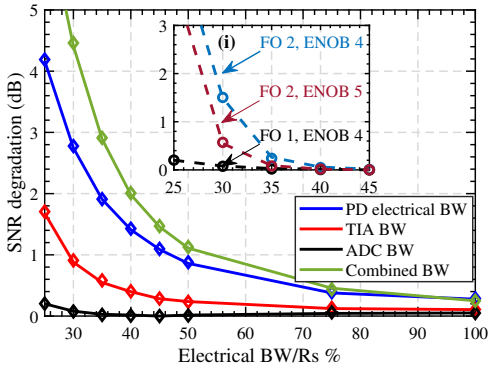

Fig. 7. SNR degradation versus CRx components individual and combined electrical 3-dB bandwidth limitation as a percentage of symbol-rate at an OSNR of 20 dB defined on a bandwidth equal to the signal symbol-rate. Inset (i): ADC bandwidth limitations considering ADC filter-order (FO) and ENOB. Lines: frequency simulator, markers: time simulator.

evaluated by the two discussed simulators, taking into account optical and electrical noises without any additional impairments. Additionally, inset (i) in Fig. 7 highlights the effect of ADC bandwidth limitations, using the same axes to represent SNR degradation (dB) versus ADC filter bandwidth relative to the symbol rate (%), while considering the impact of its filter order and ENOB. The results from the frequency simulator show excellent consistency with those obtained from the time simulator. Notably, the results reveal that when bandwidth limitations are present in all components simultaneously, the impact on the SNR penalty is most significant. For instance, a 3-dB bandwidth limitation of 35% of the symbol-rate results in a 3 dB penalty. However, when the same bandwidth limitation is applied to each component individually, the PD incurs a 2 dB penalty, while the TIA leads to a 0.4 dB penalty, and the ADC results in a negligible penalty. However, this negligible penalty can be attributed to the specific filter order employed and the low level of quantization noise following the filtering process. Nonetheless, the impact of the ADC becomes more pronounced as the filter order increases or in scenarios involving higher quantization noise levels, such as with higher modulation orders. Inset (i) of Fig. 7 illustrates this effect, showing that when the filter order is increased to 2, the SNR degradation rises to 1.5 dB for an ADC with a 3-dB bandwidth of 30% of the symbol-rate with an ENOB of 4. Increasing the ENOB, which reduces the quantization noise, mitigates this penalty by approximately 1 dB.

A.3. Coherent Receiver IQ Impairments (Amplitude, Phase imbalance and Time Skew)

In this subsection, we present examples of the frequency-domain model used to analyze impairments caused by internal imbalances within the coherent receiver, which arise due to discrepancies in the characteristics of the I and Q paths. We define the 'IQ amplitude imbalance' as the gain mismatch between the real and imaginary components. This imbalance may result, for example, from variations in PDs responsivity, where the responsivity for the I path is αR and for the Q path is R, with α representing the amplitude imbalance considered in the following analysis. Phase imbalance, on the other hand, refers to the mutual coupling between these components [21], which can be introduced through the optical hybrid parameters of the developed model, represented as $e^{j\phi}$ in the LO s parameters of Q different than I,

and thus s parameters in Eq. 15 and 19 are complex numbers. Time skew occurs when there is a time delay in the I path relative to the Q path, typically resulting from differences in the physical paths that the signals travel through, i.e. parameters ($\tau^{PI} = \tau^{NI}$) but not equal to ($\tau^{PQ} = \tau^{NQ}$) in Eq. 15 and 19.

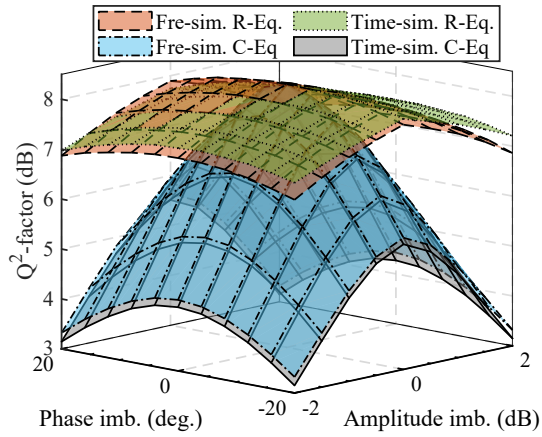

Fig. 8. Q^2 factor versus IQ phase and amplitude imbalances for a 50 Gbaud 16QAM at an OSNR of 20 dB considering both equalizers and both simulators. Fre-sim.: Frequency simulator, Time-sim.: Time simulator, R-Eq.: 4 by 4 real-valued equalizer, C-Eq.: 2 by 2 complex-valued equalizer.

We begin by evaluating the model's estimation of SNR and then the resulting Q^2 factor in the presence of IQ impairments (Q^2 factor is defined in dB as $Q^2_{dB} = 20\log_{10}\left(\sqrt{2}\text{erfcinv}\left(2BER\right)\right)$). The motivation for employing the Q^2-factor in the context of introducing IQ imbalances was to provide a basis for comparison between our modeling results and those presented in [9]. Figure 8 depicts the Q^2 factor in dB for a 50 Gbaud 16QAM signal, plotted against IQ amplitude (α in dB) and phase imbalance (ϕ), considering both frequency and time simulators for real- and complex-valued equalizers. CRx electrical and optical noises are considered, with a ROP of -27 dBm and an OSNR of 20 dB. As illustrated in Fig. 8, the Q^2 values estimated by the frequency model are consistent with the results from the time simulations for both evaluated equalizers with a maximum discrepancy of about 0.35 dB. Furthermore, the degradation in Q^2 values in the presence of IQ phase or amplitude imbalance demonstrates the inability of the 2 by 2 complex-valued equalizer to effectively compensate for IQ impairments, in contrast to the 4 by 4 real-valued equalizer. For instance, a 20 degree of phase imbalance with $\alpha = 2$ dB results in about 3.6 dB degradation in the estimated Q^2 when using a complex-valued equalizer, compared to deploying a real-valued equalizer. It should be noted that practical digital coherent receivers typically calibrate such imbalances [22]. Consequently, a calibrated coherent receiver combined with a 2×2 equalizer can achieve performance comparable to that of a 4×4 equalizer. These results, however, are primarily intended to validate the model's accuracy with both equalizers rather than to emphasize the performance improvement of the 4×4 equalizer. Furthermore, this analysis supports performance prediction by considering the low levels of residual receiver impairments with a 2×2 equalizer.

On the other hand, we evaluate, in Fig. 9, Q^2 factor with respect to time skew, expressed as a percentage of the symbol duration, for a 50 Gbaud DP-QPSK and 16QAM signals with a ROP of -27 dBm. Although this paper is not focused on comparing equalizers, and a detailed analysis of time skew in coherent receivers is available in [23, 24], the simulator results support that the performance of the 4×4 equalizer remains unaffected by IQ time skew, regardless of the modulation format. In contrast, the 2×2 equalizer experiences significant performance degradation. The results indicate that the performance of the 4 by 4 equalizer is unaffected by IQ time skew for either modulation format. In contrast, the 2 by 2 equalizer exhibits significant performance degradation, with Q^2 reductions of about 2 and 4 dB for time skews of 20% and 30% of the symbol duration in 16QAM, respectively.

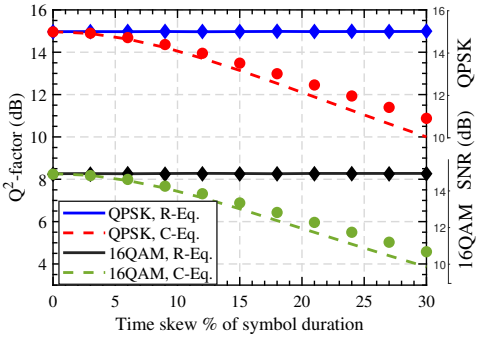

Fig. 9. Q^2 factor versus IQ time skew as a percentage of symbol duration for a 50 Gbaud QPSK and 16QAM at an OSNR of 20 dB considering both equalizers and both simulators. Lines: frequency simulator, markers: time simulator.

B. Model Validation in a Converged Metro + Passive Optical Network Setup

In this section, we assess the validity of our frequency model within a converged metro + PON network as illustrated in Fig. 2. In the proposed setup, the signal propagates through an optically amplified metro segment, represented by the concatenation of N number of ROADMs as described in [8]. Each ROADM includes two WSSs with a super-Gaussian filter profile with the order of 6 and a B GHz bandwidth [25]. The optical channel further incorporates a random unitary Jones matrix, PDL, and optical noise, which is introduced into the signal prior to the PON segment, followed by coherent detection. In this setup, we evaluate system performance using our developed frequency model, comparing it to time simulations across various network parameters. These parameters include optical filtering as well as polarization effects whether or not CRx impairments are present.

B.1. Optical Filtering

We begin by evaluating the impact of optical filtering on the PON power budget, which directly influences the PON splitter number of outputs and/or the access network reach.

Figure 10 reports the allowed loss in the optical distribution network required to achieve a BER of 10^{-2} for various OSNR values at the end of the metro segment, considering the number and the bandwidth of WSSs with a 50 Gbaud DP QPSK and 16QAM signals. Figure 10 (a) accounts only for CRx electrical noise, while Fig. 10 (b) extends the evaluation to include the effects of CRx electrical bandwidth limitations and IQ imbalances. As depicted, with up to 10 WSSs (5 ROADMS, 2 WSS per ROADM) and a filtering bandwidth of 1.2 the symbol-rate, the

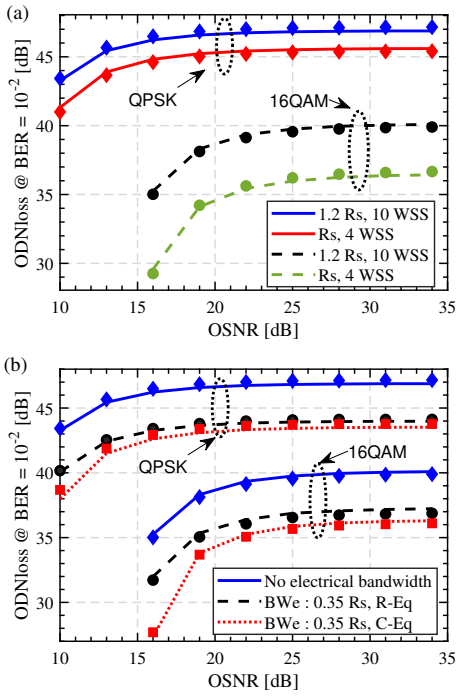

Fig. 10. Optical distribution loss allowed to achieve a BER of 10^{-2} versus OSNR for two modulation formats considering various filtering setups, (a) Optical filtering, (b) Optical filtering and CRx bandwidth limitations with IQ phase imbalance. Lines: frequency simulator, markers: time simulator.

PON can support up to 47 and 40 dB of power loss for QPSK and 16QAM, respectively, when the OSNR exceeds 20 dB in the metro segment, corresponding to bitrates of 200 Gbps and 400 Gbps. However, reducing the optical filtering bandwidth to match the symbol-rate, even with fewer WSSs such as 4, decreases the allowable PON power budget by approximately 2 dB for QPSK and 3 dB for 16QAM. In Fig. 10 (b), along with the optical filtering introduces by 10 WSSs with a bandwidth of 1.2 the symbol-rate, PD electrical bandwidth of 0.35 of the symbol-rate is applied with a phase imbalance of 20 and 10 degrees for QPSK and 16QAM, respectively. The performance of both equalizers is evaluated, revealing that with a 4 by 4 equalizer, the inclusion of CRx impairments results in a reduction of the allowed PON loss by approximately 3 dB. Furthermore, due to the introduction of phase imbalance, an extra reduction of 0.5 dB for QPSK and 1 dB for 16QAM is observed when using a 2 by 2 equalizer. Additionally, the frequency simulator shows strong agreement with time-domain simulations.

B.2. Polarization Rotation and PDL

A further example of application of our model, we evaluate the accuracy of the frequency simulator in estimating SNR and, consequently Q^2 factor, in the presence of random fiber birefringence polarization rotation and PDL along with IQ imbalances at the CRx.

Figure 11 (a) and (b) present the analysis of the Q^2 factor as a function of IQ phase imbalance for polarizations x and y, respectively, using a 50 Gbaud 16QAM signal with an OSNR of 30 dB and ROP of -20 dBm. This evaluation is performed in a converged network setup, accounting for polarization rotation and PDL, and considering both equalizers and simulators. As

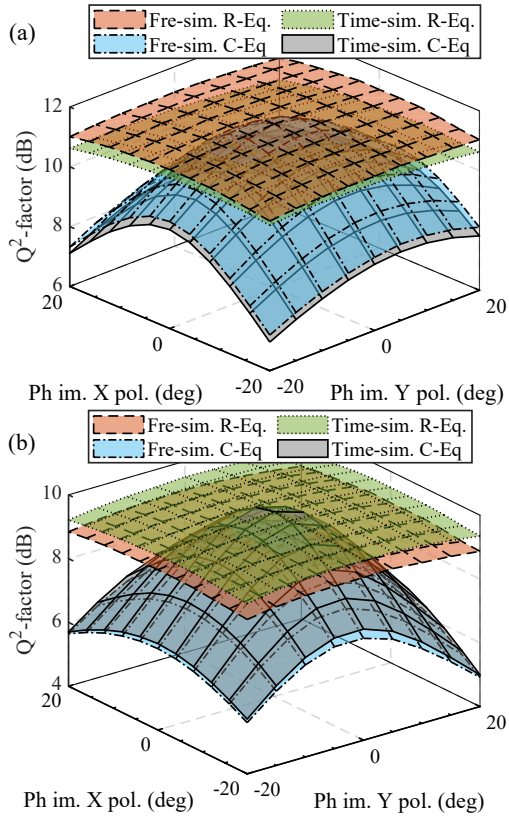

Fig. 11. Q^2 factor as a function of IQ phase imbalance on both polarizations for (a) polarization x and (b) polarization y, for a 50 Gbaud 16QAM at an OSNR of 30 dB converged network with polarization rotation and PDL considering both equalizers and both simulators. Fre-sim.: Frequency simulator, Time-sim.: Time simulator, R-Eq.: 4 by 4 real-valued equalizer, C-Eq.: 2 by 2 complex-valued equalizer.

shown, when comparing the results from the frequency and time simulators, there is a maximum discrepancy of approximately 0.5 dB in the estimated Q^2 factor for both polarizations and equalizers. In this case, we assume a given random unitary Jones matrix combined with PDL in the optical channel, which remains constant across all receiver impairments. As a result, polarization x (Fig. 11 (a)) exhibits a higher Q^2 factor compared to polarization y (Fig. 11 (b)). As expected, the 4 by 4 equalizer exhibits robust performance against phase imbalance, whereas the 2 by 2 equalizer incurs a penalty of between 3.5 and 4 dB for a -20 degrees shift on both polarizations. It is also observed that with the 2 by 2 equalizer, a phase shift in one polarization will increase the penalty in the other polarization of about 1 to 1.5 dB in Q^2 factor.

C. Statistical Accuracy of the Model

In this final validation subsection, we evaluate the statistical accuracy of the proposed frequency-resolved model by randomly varying several network parameters within their practical ranges in a Monte-Carlo simulation over 1,000 runs, and comparing the estimated SNR from the model to that obtained from time-domain simulations using both real- and complex-valued equalizers. The varied network parameters include the number of WSSs (ranging from 2 to 10) with random unitary Jones matrices, assuming a PDL_{dB} of 1 dB for each individual WSS, ROP

between −25 and −15 dBm, OSNR between 20 and 30 dB, a random IQ phase shift between 0 and 30 degrees, thermal noise between 15 to 30 pA/sqrt(Hz), and ENOB values randomly selected as 4, 5, or 6 bits. The model also accounts for other impairments such as shot noise, RIN, and PD electrical bandwidth limitations.

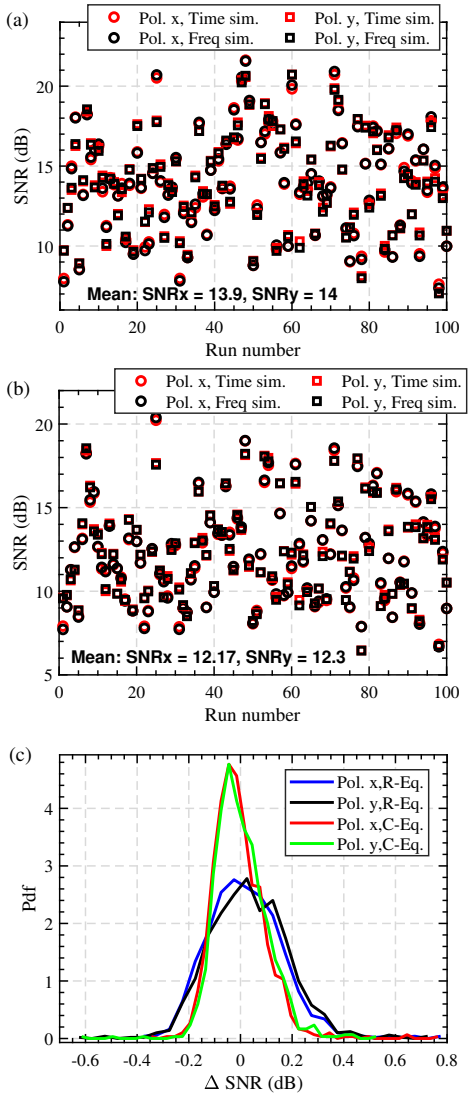

Fig. 12. SNR value estimated by the proposed frequency simulator compared to the time simulator for a 50 Gbaud DP-QPSK coherent metro + PON in both polarizations, assuming: (a) 4 by 4 real-valued equalizer, and (b) 2 by 2 complex-valued equalizer, considering random network and CRx parameters. (c) Probability density function of the SNR error between the developed frequency-resolved model and the time simulations for both polarizations and equalizers for 1000 runs.

Figure 12 (a) and (b) present the estimated SNR from both the proposed frequency-resolved model and the time-domain simulation for 100 runs, considering both polarizations and 4 by 4 and 2 by 2 equalizers, respectively. The results demonstrate strong consistency between the two simulators, with the frequency simulator showing a significant speed advantage, being 85x faster than the time-domain simulations in terms of the required CPU processing time. However, in this comparison, the frequency-domain simulator demonstrates a longer processing time than the previous example, likely due to the increased computational overhead introduced by optical and electrical filtering, and the subsequent inversion of frequency responses. The observed difference in mean SNR between real and complex equalizers, approximately 1.7 dB, is attributed to the penalty from IQ phase imbalance. To further illustrate the model's accuracy, Fig. 12 (c) shows the probability density function (pdf) of the SNR error between the frequency-resolved model and the time-domain simulations across both polarizations and equalizers over 1,000 iterations. This pdf indicates that errors have a standard deviation of about 0.15 dB, highlighting the accuracy of the frequency simulator even on such a large parameter variations.

4. PRACTICAL EXAMPLES OF MODEL APPLICATIONS

We present two applications of the proposed frequency-resolved model and its corresponding simulator, aimed at designing future flexible CPONs that support ultra-high bitrate services such as FH requirements [1]. In these applications, our goal was to assign the highest possible bitrate based on available transmission options, CRx impairments and the network parameters for each optical network unit (ONU). This first example is meant to demonstrate the promising potential of the developed model as a foundation for planning tools in flexible PON deployments, enabling the grouping of ONUs on the same wavelength according to their capabilities and requirements.

In the following analysis, we assume the metro segment consists of 10 WSSs, each with a super-Gaussian filter of the sixth order and a bandwidth of 300 GHz. The ONUs have the physical parameters specified in Sect. 3.A.1, with a LO power of 14 dBm, in addition to IQ phase imbalance of 20 degrees, which is considered a high value given the calibration and monitoring capabilities of practical transceivers, however, it is included to assist in network dimensioning and scalability by capturing both worst-case and best-case scenarios. All CRx electrical components are modeled as first-order super-Gaussian filters with a 3-dB bandwidth of 25 GHz.

A. Dimensioning of Coherent Transmission over PON Assuming Discretely-variable Bitrate Coherent Transceivers

In this first example of application, we consider the collected data on ODN loss from 4 million optical paths belonging to Orange's customers in GPON France [26] and we assume an average downstream transmitted power of 9 dBm to derive the distribution of ONU ROP. Using the proposed frequency-resolved simulator, we then analyze the network to assign the maximum achievable bitrate to each ONU (for a given BER target) by varying key transmission parameters commonly available in modern coherent transceivers, including modulation formats (QPSK or 16QAM) and symbol-rates (25 or 50 Gbaud). Additionally, within the DSP module, we examine the use of either real-valued or complex-valued equalizers, combined with forward error correction (FEC) schemes employing either soft-decision (SD) or hard-decision (HD) decoding, corresponding to a BER of 2×10^{-2} or 10^{-2}, respectively. This network dimensioning considers the metro parameters, PON power budget, CRx physical characteristics and available DSP options. Thus, the resulting bitrate assignments can subsequently assist in grouping ONUs with similar configurations to the corresponding Optical Line Terminals (OLT), providing enhanced flexibility and reconfigurability in network planning and optimization. For evaluation, we consider two OSNR values, specifically 15 and

30 dB, defined at a symbol-rate of 25 Gbaud with a ROP of −20 dBm.

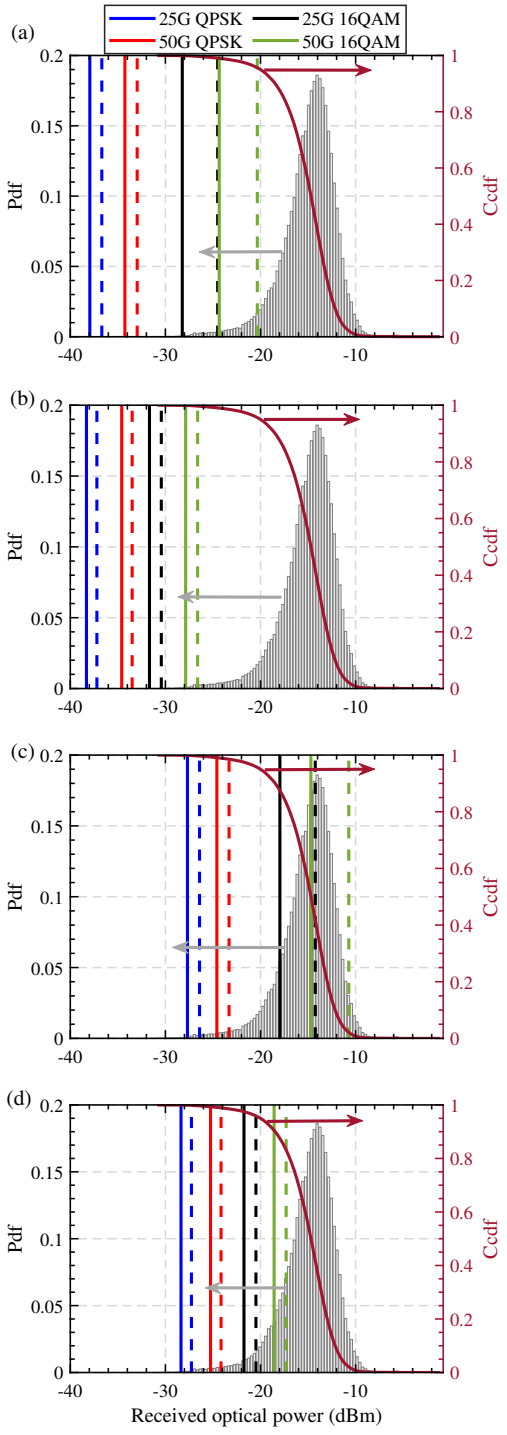

Fig. 13. Probability density function (Pdf) and complementary cumulative density function (Ccdf) of optical network units received optical power, along with vertical lines representing estimated sensitivities for an OSNR of 30 dB in metro with (a) 2 by 2 complex-valued equalizer, and (b) 4 by 4 real-valued equalizer at the CRx, and an OSNR of 15 dB with (c) 2 by 2 complex-valued equalizer. and (d) 4 by 4 real-valued equalizer. Solid lines: SD-FEC (2×10^{-2}), dashed lines: FEC with HD (10^{-2}). Legend of (a) applies to all figures.

Figure 13 presents the distribution of ROP across ONUs. Using the frequency simulator, we estimate the required sensitivity for two OSNR values: 30 dB, shown in Fig. 13 (a) and (b), and 15 dB, shown in Fig. 13 (c) and (d). The estimated sensitivity also accounts for the DSP complex-valued equalizer in Fig. 13 (a) and (c) and real-valued equalizer in Fig. 13 (b) and (d). As depicted, with an OSNR of 30 dB, all ONUs can achieve 200 Gbps using 50 Gbaud DP-QPSK. However, a 400 Gbps transmission using 50 Gbaud DP-16QAM can be supported to the majority of the ONUs (i.e. ROP higher than −24 dBm) when using complex-valued equalizers and SD-FEC, whereas ONUs with real-valued equalizers, a ROP higher than −28 dBm is required to achieve 400 Gbps. On the other hand, with an OSNR of 15 dB, all ONUs can attain 100 Gbps using 25 Gbaud DP-QPSK, and the majority (i.e. ROP higher than −25) can achieve even 200 Gbps regardless of the equalizer used. For 400 Gbps transmission with 50 Gbaud DP-16QAM with SD-FEC, a ROP greater than −14 dBm is necessary when using a complex-valued equalizer, and greater than −18 dBm when using a real-valued equalizer.

B. Future Continuous Variable Symbol-rate Coherent Transceivers

Assuming future coherent transceivers allowing an (almost) continuously variable symbol-rate (i.e., transceivers capable of adaptively adjusting the symbol rate in relatively small increments, such as 10 Gbaud, rather than being restricted to fixed rates like 25 Gbaud or 50 Gbaud), we estimate the maximum achievable bitrate by considering two modulation formats, the two considered equalizers, and both SD- and HD-FEC. For this analysis, we retain the previous network and CRx specifications, while setting the OSNR at 30 dB for a symbol-rate of 25 Gbaud, with a ROP of −20 dBm.

Figure 14 illustrates the estimated maximum achievable bitrate with respect to ROP considering a variable symbol-rate. We evaluate two modulation formats, QPSK and 16QAM, paired with a real-valued and complex-valued equalizer in Fig. 14 (a) and (b), respectively. As seen, even with a low ROP, such as −30 dBm, rates of 300 Gbps can be achieved with a variable symbol-rate and coherent PON, reaching up to 700 Gbps for a ROP of −10 dBm. For both equalizers, QPSK outperforms 16QAM at lower ROP values, but after a certain threshold (−27 dBm for the 4×4 real-valued equalizer and −22 dBm for the 2×2 complex-valued equalizer) 16QAM supports higher bitrates. It is also shown that, even with increasing ROP and symbol-rate, bitrates reach a maximum value (such as 440 Gbps for QPSK), likely due to electrical bandwidth limitations. Additionally, the results highlight the trade-offs between increasing complexity by equalizer and FEC type and improving system performance, offering valuable insights for the design of next-generation coherent PON systems. Finally, Fig. 14 (c) depicts the distribution of the ROP along with the maximum possible bitrate under the discussed transmission conditions with highest DSP capabilities (FEC-SD and 4 by 4 real-valued equalizer). As shown, with a variable symbol-rate, approximately 85% of the ONUs can be supported with 640 Gbps, while 10% (i.e. ROP higher than −12 dBm) can attain 720 Gbps.

5. DISCUSSION AND CONCLUSIONS

In this paper, we developed an analytical frequency-resolved model to estimate the performance of coherent transmission and then we propose its use over a converged metro + PON network, accounting for a wide range of optical and electrical impair-

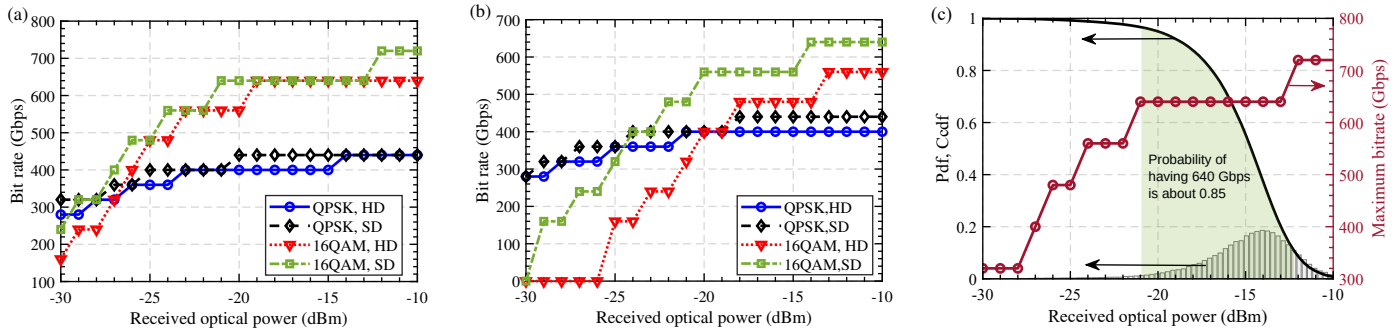

Fig. 14. Maximum achievable bitrates versus received optical power in a future flexible symbol-rate coherent transmission with (a) 4 by 4 real-valued equalizer, (b) 2 by 2 complex-valued equalizer. (c) Maximum supported bitrate corresponding to today's distribution of received optical power.

ments. The model is thoroughly validated through comparison with accurate but highly CPU-time consuming time-domain simulations, demonstrating a discrepancy in the estimated SNR with a standard deviation of about 0.15 dB based on statistical accuracy analysis across various transmission non-idealities.

We then show application of the model to several future but practical PON or metro+PON scenarios targeting ultra high bit rate transmission. Results indicate that future coherent PON systems with today's transceivers can support bitrates of 200 Gbps for most ONUs, with the potential for 400 Gbps in certain cases. Moreover, under specific conditions—such as metro segment specifications, OSNR levels, PON losses, and practical coherent receiver impairments—the model was shown to be able to estimate the maximum achievable bitrate by incorporating a continuously variable symbol-rate. Additionally, based on the distribution for ONUs' ROP, it further predicts that about 85% of ONUs could support bitrates up to 640 Gbps. From an application point of view, these bitrates may today be perceived as excessively high in the access segments. Anyway, as discussed for instance in [1] for the medium to long term, the support of future 6G fronthauling solutions using massive MIMO and very large RF bandwidths may sooner or later mandates for multi gigabit/s also in fiber access. If and when this happen, our model may become a valuable foundation for physical-aware network planning and optimization tools, enabling operators to efficiently design, optimize, and scale ultra-high speed future CPON services.

As a last observation, even though all the application examples presented here are in the metro+PON scenario, we believe that the proposed model, when joined with all the existing literature on nonlinear fiber propagation effects modeled as additional GN-models and thus G-OSNR, can potentially be applicable also to other areas using coherent transmission. Our future work will also focus on incorporating transmitter impairments into the model such as IQ imbalances (amplitude, phase and time skew), and bandwidth limitations. Extending its application to digital subcarrier multiplexing systems can also be considered.

APPENDIX A

To obtain the I component differential current in Eq. 6, we substitute Eq. 4 and Eq. 5 as follows:

$$\begin{aligned}
&\Delta i^I(t) = i^{PI}(t) - i^{NI}(t) = \\
&2\left(h^{PI}\left(t-\tau^{PI}\right)R^{PI}\Re\left\{s^{PI}\right\}+h^{NI}\left(t-\tau^{NI}\right)R^{NI}\Re\left\{s^{NI}\right\}\right) \\
&\otimes \Re\left\{E_S E_L^*\right\} - 2\left(h^{PI}\left(t-\tau^{PI}\right)R^{PI}\Im\left\{s^{PI}\right\}\right. \\
&\left.+h^{NI}\left(t-\tau^{NI}\right)R^{NI}\Im\left\{s^{NI}\right\}\right)\otimes\Im\left\{E_S E_L^*\right\} \\
&+2\left(h^{PI}\left(t-\tau^{PI}\right)R^{PI}\Re\left\{s^{PI}\right\}+h^{NI}\left(t-\tau^{NI}\right)R^{NI}\Re\left\{s^{NI}\right\}\right) \\
&\otimes \Re\left\{E_{NO} E_L^*\right\} - 2\left(h^{PI}\left(t-\tau^{PI}\right)R^{PI}\Im\left\{s^{PI}\right\}\right. \\
&\left.+h^{NI}\left(t-\tau^{NI}\right)R^{NI}\Im\left\{s^{NI}\right\}\right)\otimes\Im\left\{E_{NO} E_L^*\right\} \\
&+\left(h^{PI}\left(t-\tau^{PI}\right)R^{PI}\left|s_2^{PI}\right|^2 - h^{NI}\left(t-\tau^{NI}\right)R^{NI}\left|s_2^{NI}\right|^2\right)\otimes|E_L|^2,
\end{aligned} \tag{15}$$

which allows us to define the following:

$$\begin{aligned}
&h_{BPD}^{II} = \\
&2\left(h^{PI}\left(t-\tau^{PI}\right)R^{PI}\Re\left\{s^{PI}\right\}+h^{NI}\left(t-\tau^{NI}\right)R^{NI}\Re\left\{s^{NI}\right\}\right),
\end{aligned} \tag{16}$$

$$\begin{aligned}
&h_{BPD}^{IQ} = \\
&-2\left(h^{PI}\left(t-\tau^{PI}\right)R^{PI}\Im\left\{s^{PI}\right\}+h^{NI}\left(t-\tau^{NI}\right)R^{NI}\Im\left\{s^{NI}\right\}\right),
\end{aligned} \tag{17}$$

$$h_{LO}^{I} = \left(h^{PI}\left(t-\tau^{PI}\right)R^{PI}\left|s_2^{PI}\right|^2 - h^{NI}\left(t-\tau^{NI}\right)R^{NI}\left|s_2^{NI}\right|^2\right), \tag{18}$$

Similarly for the Q component differential current in Eq. 7:

$$\begin{aligned}
&\Delta i^{Q}(t) = i^{PQ}(t) - i^{NQ}(t) = \\
&2\left(h^{PQ}\left(t-\tau^{PQ}\right)R^{PQ}\Re\left\{s^{PQ}\right\} + h^{NQ}\left(t-\tau^{NQ}\right)R^{NQ}\Re\left\{s^{NQ}\right\}\right) \\
&\otimes \Im\left\{E_S E_L^*\right\} + 2\left(h^{PQ}\left(t-\tau^{PQ}\right)R^{PQ}\Im\left\{s^{PQ}\right\}\right. \\
&\left.+h^{NQ}\left(t-\tau^{NQ}\right)R^{NQ}\Im\left\{s^{NQ}\right\}\right) \otimes \Re\left\{E_S E_L^*\right\} \\
&+2\left(h^{PQ}\left(t-\tau^{PQ}\right)R^{PQ}\Re\left\{s^{PQ}\right\} + h^{NQ}\left(t-\tau^{NQ}\right)R^{NQ}\Re\left\{s^{NQ}\right\}\right) \\
&\otimes \Im\left\{E_{NO} E_L^*\right\} + 2\left(h^{PQ}\left(t-\tau^{PQ}\right)R^{PQ}\Im\left\{s^{PQ}\right\}\right. \\
&\left.+h^{NQ}\left(t-\tau^{NQ}\right)R^{NQ}\Im\left\{s^{NQ}\right\}\right) \otimes \Re\left\{E_{NO} E_L^*\right\} \\
&+\left(h^{PQ}\left(t-\tau^{PQ}\right)R^{PQ}\left|s_2^{PQ}\right|^2 - h^{NQ}\left(t-\tau^{NQ}\right)R^{NQ}\left|s_2^{NQ}\right|^2\right)\otimes|E_L|^2,
\end{aligned} \tag{19}$$

and consequently defining:

$$\begin{aligned}
&h_{BPD}^{QI} = \\
&2\left(h^{PQ}\left(t-\tau^{PQ}\right)R^{PQ}\Im\left\{s^{PQ}\right\} + h^{NQ}\left(t-\tau^{NQ}\right)R^{NQ}\Im\left\{s^{NQ}\right\}\right),
\end{aligned} \tag{20}$$

$$\begin{aligned}
&h_{BPD}^{QQ} = \\
&2\left(h^{PQ}\left(t-\tau^{PQ}\right)R^{PQ}\Re\left\{s^{PQ}\right\} + h^{NQ}\left(t-\tau^{NQ}\right)R^{NQ}\Re\left\{s^{NQ}\right\}\right),
\end{aligned} \tag{21}$$

$$h_{LO}^{Q} = \left(h^{PQ}\left(t-\tau^{PQ}\right)R^{PQ}\left|s_2^{PQ}\right|^2 - h^{NQ}\left(t-\tau^{NQ}\right)R^{NQ}\left|s_2^{NQ}\right|^2\right), \tag{22}$$

Thus $\mathbf{h}_{BPD}$ is defined as:

$$\begin{aligned}
&\begin{bmatrix} \Delta i^{I,x}(t) \\ \Delta i^{Q,x}(t) \\ \Delta i^{I,y}(t) \\ \Delta i^{Q,y}(t) \end{bmatrix} = \underbrace{\begin{bmatrix} h_{BPD}^{II,x}(t) & h_{BPD}^{IQ,x}(t) & 0 & 0 \\ h_{BPD}^{QI,x}(t) & h_{BPD}^{QQ,x}(t) & 0 & 0 \\ 0 & 0 & h_{BPD}^{II,y}(t) & h_{BPD}^{IQ,y}(t) \\ 0 & 0 & h_{BPD}^{QI,y}(t) & h_{BPD}^{QQ,y}(t) \end{bmatrix}}_{\mathbf{h}_{BPD}} \\
&\otimes\sqrt{P_L}\left(\begin{bmatrix} I^x(t) \\ Q^x(t) \\ I^y(t) \\ Q^y(t) \end{bmatrix}_S + \begin{bmatrix} I^x(t) \\ Q^x(t) \\ I^y(t) \\ Q^y(t) \end{bmatrix}_{NO}\right) + \begin{bmatrix} h_{LO}^{I,x}(t)\otimes\left|E_L^x\right|^2 \\ h_{LO}^{Q,x}(t)\otimes\left|E_L^x\right|^2 \\ h_{LO}^{I,y}(t)\otimes\left|E_L^y\right|^2 \\ h_{LO}^{Q,y}(t)\otimes\left|E_L^y\right|^2 \end{bmatrix}
\end{aligned} \tag{23}$$

whereas $\mathbf{h}_{TIA}$ is defined as:

$$\mathbf{h}_{TIA} = \mathrm{diag}\left(h_{TIA}^{I,x}(t), h_{TIA}^{Q,x}(t), h_{TIA}^{I,y}(t), h_{TIA}^{Q,y}(t)\right), \tag{24}$$

and $\mathbf{h}_{ADC}$ is defined as:

$$\mathbf{h}_{ADC} = \mathrm{diag}\left(h_{ADC}^{I,x}(t), h_{ADC}^{Q,x}(t), h_{ADC}^{I,y}(t)\, h_{ADC}^{Q,y}(t)\right), \tag{25}$$

The combination of these three matrices, $\sqrt{P_L}\mathbf{h}_{ADC}\otimes\mathbf{h}_{TIA}\otimes\mathbf{h}_{BPD}$, defines the CRx response in terms of the in-phase and quadrature components of the CRx input and output. The resulting matrix is then transformed to derive the 4-D $\mathbf{h}_{RX}(t)$ using the widely linear representation as:

$$\mathbf{h}_{RX}(t) = \begin{bmatrix} h_1^x(t) & h_2^x(t) & 0 & 0 \\ h_2^{x*}(t) & h_1^{x*}(t) & 0 & 0 \\ 0 & 0 & h_1^y(t) & h_2^y(t) \\ 0 & 0 & h_2^{y*}(t) & h_1^{y*}(t) \end{bmatrix} \tag{26}$$

where $h_1(t)$ and $h_2(t)$ are defined as:

$$\begin{aligned}
&h_1(t) = \sqrt{P_L}h_{ADC}^I(t)\otimes h_{TIA}^I(t)\otimes\left(h^{PI}\left(t-\tau^{PI}\right)R^{PI}s^{PI}\right. \\
&\left.+h^{NI}\left(t-\tau^{NI}\right)R^{NI}s^{NI}\right) + \sqrt{P_L}h_{ADC}^Q(t)\otimes h_{TIA}^Q(t)\otimes \\
&\left(h^{PQ}\left(t-\tau^{PQ}\right)R^{PQ}s^{PQ} + h^{NQ}\left(t-\tau^{NQ}\right)R^{NQ}s^{NQ}\right)
\end{aligned} \tag{27}$$

$$\begin{aligned}
&h_2(t) = \sqrt{P_L}h_{ADC}^I(t)\otimes h_{TIA}^I(t)\otimes\left(h^{PI}\left(t-\tau^{PI}\right)R^{PI}s^{PI*}\right. \\
&\left.+h^{NI}\left(t-\tau^{NI}\right)R^{NI}s^{NI*}\right) - \sqrt{P_L}h_{ADC}^Q(t)\otimes h_{TIA}^Q(t)\otimes \\
&\left(h^{PQ}\left(t-\tau^{PQ}\right)R^{PQ}s^{PQ*} + h^{NQ}\left(t-\tau^{NQ}\right)R^{NQ}s^{NQ*}\right)
\end{aligned} \tag{28}$$

The CRx noises are defined as:

$$\begin{aligned}
&\mathbf{n}_{RX}(t) = \begin{bmatrix} n_{RX}^x(t) \\ n_{RX}^{x*}(t) \\ n_{RX}^y(t) \\ n_{RX}^{y*}(t) \end{bmatrix} = \underbrace{\begin{bmatrix} 1 & j & 0 & 0 \\ 1 & -j & 0 & 0 \\ 0 & 0 & 1 & j \\ 0 & 0 & 1 & -j \end{bmatrix}}_{T}\begin{bmatrix} n_{RX}^{I,x}(t) \\ n_{RX}^{Q,x}(t) \\ n_{RX}^{I,y}(t) \\ n_{RX}^{Q,y}(t) \end{bmatrix} \\
&= \mathbf{T}\mathbf{h}_{ADC}(t)\otimes\mathbf{h}_{TIA}(t)\otimes \\
&\left(\begin{bmatrix} h_{LO}^{I,x}(t)\otimes\left|E_L^x\right|^2 \\ h_{LO}^{Q,x}(t)\otimes\left|E_L^x\right|^2 \\ h_{LO}^{I,y}(t)\otimes\left|E_L^y\right|^2 \\ h_{LO}^{Q,y}(t)\otimes\left|E_L^y\right|^2 \end{bmatrix} + \begin{bmatrix} n_{sh}^{I,x}(t) \\ n_{sh}^{Q,x}(t) \\ n_{sh}^{I,y}(t) \\ n_{sh}^{Q,y}(t) \end{bmatrix}\right) \\
&+\mathbf{T}\mathbf{h}_{ADC}(t)\otimes\begin{bmatrix} n_{th}^{I,x}(t) \\ n_{th}^{Q,x}(t) \\ n_{th}^{I,y}(t) \\ n_{th}^{Q,y}(t) \end{bmatrix} + \mathbf{T}\begin{bmatrix} n_{ADC}^{I,x}(t) \\ n_{ADC}^{Q,x}(t) \\ n_{ADC}^{I,y}(t) \\ n_{ADC}^{Q,y}(t) \end{bmatrix},
\end{aligned} \tag{29}$$

To form $\mathbf{H}^{-1}(f)$, we start by writing the overall 4-D response $\mathbf{H}(f)$ as:

$$\mathbf{H}(f) = \mathbf{H}_{RX}(f)\,\mathbf{H}_s(f) = \begin{bmatrix} H_{11} & H_{12} & H_{13} & H_{14} \\ H_{21} & H_{22} & H_{23} & H_{24} \\ H_{31} & H_{32} & H_{33} & H_{34} \\ H_{41} & H_{42} & H_{43} & H_{44} \end{bmatrix} \tag{30}$$

Then, we extract only the components that are processed by the 2 by 2 equalizer as follows:

$$\mathbf{C}(f) = \begin{bmatrix} H_{11} & H_{13} \\ H_{31} & H_{33} \end{bmatrix} \tag{31}$$

which yields its inverse to be:

$$\mathbf{C^{-1}}(f) = \begin{bmatrix} C_{11} & C_{13} \\ C_{31} & C_{33} \end{bmatrix} \tag{32}$$

Finally, we can write:

$$\mathbf{H}^{-1}(f) = \begin{bmatrix} C_{11} & 0 & C_{13} & 0 \\ 0 & 0 & 0 & 0 \\ C_{31} & 0 & C_{33} & 0 \\ 0 & 0 & 0 & 0 \end{bmatrix} \tag{33}$$

FUNDING

HORIZON EUROPE Marie Sklodowska-Curie Actions (101073265).

ACKNOWLEDGMENTS

This work has received funding from the European Union's Horizon Europe research and innovation programme under the Marie Skłodowska-Curie grant agreement No. 101073265 (EWOC). Views and opinions expressed are however those of the authors only and do not necessarily reflect those of the European Union. The European Union cannot be held responsible for them.

REFERENCES

1. Z. Vujicic, M. C. Santos, R. Méndez, B. Klaiqi, J. Rodriguez, X. Gelabert, M. A. Rahman, and R. Gaudino, "Toward virtualized optical-wireless heterogeneous networks," IEEE Access **12**, 87776–87806 (2024).
2. S. Alzoubi, S. Arnaout, M. A. Rahman, and R. Gaudino, "Future evolutions of fronthauling architectures over passive optical networks," in *2024 24th International Conference on Transparent Optical Networks (ICTON),* (2024), pp. 1–4.
3. G. Rizzelli, M. Casasco, A. Pagano, V. Ferrero, and R. Gaudino, "Experimental demonstration of in-field 400G coherent metro-access convergence," in *Optical Fiber Communication Conference (OFC) 2024,* (Optica Publishing Group, 2024), p. W1J.1.
4. P. Torres-Ferrera, F. Effenberger, M. S. Faruk, S. J. Savory, and R. Gaudino, "Overview of high-speed TDM-PON beyond 50 Gbps per wavelength using digital signal processing [invited tutorial]," J. Opt. Commun. Netw. **14**, 982–996 (2022).
5. H. Zhang, Z. Jia, L. A. Campos, and C. Knittle, "Experimental demonstration of rate-flexible coherent PON up to 300 Gb/s," J. Light. Technol. **42**, 5440–5449 (2024).
6. Q. Zhuge, X. Liu, Y. Zhang, M. Cai, Y. Liu, Q. Qiu, X. Zhong, J. Wu, R. Gao, L. Yi, and W. Hu, "Building a digital twin for intelligent optical networks [invited tutorial]," J. Opt. Commun. Netw. **15**, C242–C262 (2023).
7. M. S. Faruk and S. J. Savory, "Measurement informed models and digital twins for optical fiber communication systems," J. Light. Technol. **42**, 1016–1030 (2024).
8. G. Rizzelli, P. Torres-Ferrera, and R. Gaudino, "An analytical model for coherent transmission performance estimation after generic jones matrices," J. Light. Technol. **41**, 4582–4589 (2023).
9. E. P. da Silva and D. Zibar, "Widely linear equalization for IQ imbalance and skew compensation in optical coherent receivers," J. Light. Technol. **34**, 3577–3586 (2016).
10. J. S. Fandino and P. Munoz, "Manufacturing tolerance analysis of an MMI-based 90° optical hybrid for InP integrated coherent receivers," IEEE Photonics J. **5**, 7900512–7900512 (2013).
11. M. Morsy-Osman, M. Chagnon, X. Xu, Q. Zhuge, M. Poulin, Y. Painchaud, M. Pelletier, C. Paquet, and D. V. Plant, "Analytical and experimental performance evaluation of an integrated Si-photonic balanced coherent receiver in a colorless scenario," Opt. Express **22**, 5693–5730 (2014).
12. R. F. Fischer, *Precoding and signal shaping for digital transmission* (John Wiley & Sons, 2005).
13. P. Rykaczewski, M. Valkama, and M. Renfors, "On the connection of I/Q imbalance and channel equalization in direct-conversion transceivers," IEEE Transactions on Veh. Technol. **57**, 1630–1636 (2008).
14. D. Pilori, M. Cantono, A. Carena, and V. Curri, "FFSS: The fast fiber simulator software," in *2017 19th International Conference on Transparent Optical Networks (ICTON),* (2017), pp. 1–4.
15. K. Cho and D. Yoon, "On the general BER expression of one- and two-dimensional amplitude modulations," IEEE Transactions on Commun. **50**, 1074–1080 (2002).
16. B. Zhang, C. Malouin, and T. J. Schmidt, "Design of coherent receiver optical front end for unamplified applications," Opt. express **20**, 3225–3234 (2012).
17. A. Napoli, M. M. Mezghanni, T. Rahman, D. Rafique, R. Palmer, B. Spinnler, S. Calabrò, C. Castro, M. Kuschnerov, and M. Bohn, "Digital compensation of bandwidth limitations for high-speed DACs and ADCs," J. Light. Technol. **34**, 3053–3064 (2016).
18. S. Daumont, B. Rihawi, and Y. Lout, "Root-raised cosine filter influences on PAPR distribution of single carrier signals," in *2008 3rd International Symposium on Communications, Control and Signal Processing,* (2008), pp. 841–845.
19. C. Xie, "Chromatic dispersion estimation for single-carrier coherent optical communications," IEEE Photonics Technol. Lett. **25**, 992–995 (2013).
20. G. R. Martella, A. Nespola, S. Straullu, F. Forghieri, and R. Gaudino, "Scaling laws for unamplified coherent transmission in next-generation short-reach and access networks," J. Light. Technol. **39**, 5805–5814 (2021).
21. M. S. Faruk and K. Kikuchi, "Compensation for in-phase/quadrature imbalance in coherent-receiver front end for optical quadrature amplitude modulation," IEEE Photonics J. **5**, 7800110–7800110 (2013).
22. J. Liang, Y. Fan, Z. Tao, X. Su, and H. Nakashima, "Transceiver imbalances compensation and monitoring by receiver DSP," J. Light. Technol. **39**, 5397–5404 (2021).
23. M. Paskov, D. Lavery, and S. J. Savory, "Blind equalization of receiver in-phase/quadrature skew in the presence of nyquist filtering," IEEE Photonics Technol. Lett. **25**, 2446–2449 (2013).
24. R. Rios-Müller, J. Renaudier, and G. Charlet, "Blind receiver skew compensation and estimation for long-haul non-dispersion managed systems using adaptive equalizer," J. Light. Technol. **33**, 1315–1318 (2015).
25. M. Pfennigbauer and P. Winzer, "Choice of MUX/DEMUX filter characteristics for NRZ, RZ, and CSRZ DWDM systems," J. Light. Technol. **24**, 1689–1696 (2006).
26. G. Simon, P. Chanclou, F. Saliou, J. Potet, and M. Wang, "Clustering G-PON field data to improve flexibility in next generation PON systems," in *2021 European Conference on Optical Communication (ECOC),* (2021), pp. 1–4.